

Geophysical Research Letters



RESEARCH LETTER

10.1029/2021GL093225

Special Section:

Southern Ocean clouds, aerosols, precipitation and radiation

Key Points:

- The cloud top layer within individual cloud objects frequently consists of both liquid and ice pixels
- Large cloud droplets are associated with high ice-cloud fraction and high ice optical thickness
- For ice fraction lower than 0.5, the ice fraction increases with an increase in the ice pixel pocket concentration

Supporting Information:

Supporting Information may be found in the online version of this article.

Correspondence to:

Q. Coopman,
quentin.coopman@kit.edu

Citation:

Coopman, Q., Hoose, C., & Stengel, M. (2021). Analyzing the thermodynamic phase partitioning of mixed phase clouds over the Southern Ocean using passive satellite observations. *Geophysical Research Letters*, 48, e2021GL093225. <https://doi.org/10.1029/2021GL093225>

Received 28 OCT 2020

Accepted 17 MAR 2021

Analyzing the Thermodynamic Phase Partitioning of Mixed Phase Clouds Over the Southern Ocean Using Passive Satellite Observations

Q. Coopman¹ , C. Hoose¹ , and M. Stengel² 

¹Institute of Meteorology and Climate Research, Karlsruhe Institute of Technology, Karlsruhe, Germany, ²Deutscher Wetterdienst (DWD), Offenbach, Germany

Abstract The thermodynamic phase transition of clouds is still not well understood, therefore, the partitioning of ice and liquid in mixed phase clouds is often misrepresented in numerical models. We use 12 years of cloud observations from the geostationary Spinning Enhanced Visible and InfraRed Imager over the Southern Ocean to detect clouds which contain both liquid and ice pixels at their tops and we retrieve microphysical and radiative properties in each cloud object. The results show that large cloud droplet effective radius coincides with high ice fraction and high ice optical thickness for cloud top temperatures higher than -8°C . We also found that the density of ice pixel clusters increases with the cloud ice fraction, for ice fraction lower than 0.5, suggesting a multiplication of ice pockets in line with previous studies, particularly efficient for clouds with high perimeter fractal dimension.

Plain Language Summary Clouds with coexisting liquid droplets and ice crystals are frequent but they are still not well understood and often misrepresented in numerical models. We analyze the temperature, the optical properties of clouds, and the size of droplets and ice crystals from 12 years of satellite observations over the Southern Ocean. We find that clouds with large droplets are more likely to undergo glaciation than clouds with small droplets and that at temperatures higher than -8°C the glaciation is probably associated with a higher concentration of ice crystals. We also analyze how liquid and ice are spatially distributed within clouds and we highlight that multiple ice pockets are formed when clouds glaciate rather than spreading from one ice pocket to the entire cloud. A better understanding of clouds allows a better representation of their interaction with the environment and therefore their impact on the climate. Clouds precipitate more easily if they consist of ice crystals, potentially reducing the lifetime of clouds and impacting the radiation balance at the surface and top of the atmosphere. Also, the spatial distribution of ice and liquid in clouds impacts how ice crystals and liquid droplets interact with each other.

1. Introduction

The thermodynamic cloud phase transition from liquid to ice impacts the optical and microphysical properties (Sun & Shine, 1994), the occurrence of precipitation (Mülmenstädt et al., 2015), and absorption and scattering of incoming solar and emitted infrared radiation (Tan et al., 2016). Cloud droplets homogeneously freeze at temperatures lower than -37°C but aerosols can act as ice nucleating particles so that supercooled droplets freeze at temperature between -37°C and 0°C .

Clouds can contain simultaneously liquid droplets and ice crystals. Mixed phase clouds are present from the tropics to the poles and concern a wide variety of cloud types or meteorological conditions (Shupe et al., 2008; Tan et al., 2014): Mixed phase clouds can be stratiform over oceans or associated with deep convective clouds in the Tropics (Korolev et al., 2017). However, numerical models do not represent well supercooled and mixed phase clouds causing biases in climate models (Bodas-Salcedo et al., 2016; McCoy et al., 2016) and reanalyzes (Naud et al., 2014; Stengel et al., 2018) due to a lack of observations and understanding, and resulting misrepresentation of cloud microphysics.

McCoy and Hartmann (2015) have shown that the partitioning between ice and liquid in mixed phase clouds in a warming climate contributes to at least 20%–80% of the increase in liquid water path according to 19 coupled models. Tan et al. (2016) estimated that the equilibrium climate sensitivity can be 1.3°C

© 2021. The Authors.

This is an open access article under the terms of the [Creative Commons Attribution License](https://creativecommons.org/licenses/by/4.0/), which permits use, distribution and reproduction in any medium, provided the original work is properly cited.

higher for simulations in which the phase partitioning is constrained by satellite observations. The authors have also shown that the cloud glaciation process is sensitive to the spatial distribution of phase within the clouds, that is, the presence of ice and liquid pockets or homogeneously mixed ice crystals and liquid droplets (Tan & Storelvmo, 2016).

The Southern Ocean is one of the cloudiest region on Earth and the frequency of mixed phase clouds is high (Korolev et al., 2017; Wang et al., 2003). The cloud thermodynamic phase partitioning has been determined as essential to simulate and quantify the cloud radiative impact in the Southern Ocean (Vergara-Temprado et al., 2018). Gettelman and Sherwood (2016) attributed the cloud phase as a key process to determine cloud feedback effect in the Southern Ocean. Many field campaigns took place in the Southern Ocean to study cloud microphysical and radiative properties (McFarquhar et al., 2020). Mace, Protat, et al. (2020) have shown that Southern Ocean clouds tend to be thicker with smaller and more numerous hydrometeors than other latitudes. With airborne measurements, Ahn et al. (2017) showed that 38.5% of the clouds contained ice, mainly from mixed-phase clouds, and they suggested that these clouds were considered as ideal for the Hallet-Mossop secondary ice production process.

Mace, Benson, and Hu (2020) studied mixed phase clouds in the Southern Ocean with active satellite measurements and showed that they are associated with precipitation, suggesting efficient secondary ice processes. Noh et al. (2019) developed an algorithm to study the mixed phase clouds using passive satellite observations. Korolev et al. (2017) differentiate mixed-phase clouds using different scales from in situ, active remote sensing and passive remote sensing observations. They highlighted that there is not a consensus to define mixed-phase clouds and it depends on the considered instruments. In situ and radar data have smaller averaging scale than passive satellite observations, thus they are difficult to compare.

All the different cited studies analyzed the vertical structure of clouds to define the mixed phase category. Horizontal cloud phase inhomogeneities have not been in the focus of analyses for any Southern Ocean campaign to our knowledge, in contrast to arctic clouds (Curry et al., 2000; Schäfer et al., 2018). Since the phase partitioning and the spatial distribution of the ice and liquid within clouds are important for the radiative properties and the evolution of clouds but not well understood nor represented in numerical models, we take a new perspective and we consider the horizontal inhomogeneity on cloud top to define the mixed-phase category. The present study analyses how clouds transition from mainly liquid to mainly ice. We also aim to describe and quantify the impact of cloud parameters on the ice fraction and we speculate about the potential reasons. We use 12 years of mixed phase cloud properties from a passive space-based sensor over the Southern Ocean and we analyze the ice and liquid fraction at the cloud top for each cloud for different regimes of cloud droplet radius, optical thickness, and cloud top temperature. The study does not aim to retrieve liquid and ice properties within the same pixel, but rather considering mixed-phase clouds at the pixel scale, considering the pixel as strictly liquid or ice. We also analyze the spatial distribution of ice and liquid pixels within mixed phase cloud top to understand how clouds evolve from dominantly liquid to dominantly ice.

2. Data Sets

The Spinning Enhanced Visible and Infrared Imager (SEVIRI), on board the geostationary METEOSAT second generation satellites, provides measurements with a temporal resolution of 15 min and measures in the visible and infrared. The SEVIRI disk is centered at 0° and covers the European and African continents and parts of the eastern edge of South America. The spatial resolution is 3 km at the sub-satellite point for 11 channels in the visible and infrared and for the High Resolution Visible (HRV) channel the resolution is 1 km at the sub-satellite point. The CCloud property dAtAset using SEVIRI - edition 2 (CLAAS-2, Benas et al., 2017; Stengel et al., 2014) retrieves cloud properties from recalibrated measurements following Meirink et al. (2013). The data set does not include measurements with a solar zenith and viewing zenith angles greater than 84° to mitigate potential uncertainties (Grosvenor & Wood, 2014) (See Text S1 in the supporting information for more details). Details are given in Benas et al. (2017) but we summarize hereafter the methods used to retrieve parameters relevant to our study.

Cloud top pressure uses the infrared measurements compared with clear-sky and cloudy radiative transfer simulations from the Radiative Transfer model for Television infrared observation satellite Operational

Vertical sounder (RTTOV; Matricardi et al., 2004; Saunders et al., 1999) using ERA-Interim (Dee et al., 2011) as input. The H₂O infrared window intercept method (Schmetz et al., 1993) is applied with the radiance rationing method (Menzel et al., 1983). Cloud top temperature (CTT) is retrieved from cloud top pressure via ERA-Interim temperature profiles.

The cloud top phase is determined by a decision tree using a combination of five spectral channels from 6.2 to 13.4 μm and simulated clear and cloudy sky radiances from RTTOV. The decision tree classifies cloud phase into six categories: liquid, supercooled, opaque ice, cirrus, overlap, and overshooting. The six categories are converted to liquid or ice (Benas et al., 2017).

Cloud droplet effective radius (r_e^{liq}), ice crystal effective radius (r_e^{ice}), and cloud optical thickness (τ) are determined using a bi-spectral technique (Nakajima & King, 1990) based on the channels at 0.6 and 1.6 μm (Meirink & van Zadelhoff, 2016; Roebeling et al., 2006) and the double adding KNMI radiative transfer model (Stammes, 2001).

For our analysis, we use instantaneous CLAAS-2 data at native spatiotemporal SEVIRI resolution and projection from 2004 to 2015.

3. Method

We define cloud objects as clusters of fully cloudy pixels surrounded by clear sky and we consider cloud objects containing both liquid and ice pixels at cloud tops: These clouds are considered in this study as mixed phase, but it is important to note that it does not include vertically mixed-phase clouds, for example, liquid top with ice below clouds. We set a minimum size for the considered cloud objects of 30 pixels (a schematic of a typical cloud and examples of such clouds observed by SEVIRI are shown in Figure S1 in the supporting information and described in Text S2).

Mace and Protat (2018) have shown from field campaign measurements that cloud occurrence in the Southern Ocean is dominated by low-level layers but high clouds can also be present. Only cloud objects with a difference in top temperature of less than 10 °C are considered in order to exclude multi-layer clouds detected as one cloud object. The choice for the threshold is ad-hoc but represent a good compromise between the number of analyzed cloud objects avoiding multilayer clouds. We determine the cloud properties associated with each cloud object: the mean CTT, the mean r_e^{liq} and r_e^{ice} , the mean τ for the liquid and ice pixels, and the ice fraction defined as:

$$\chi_{ice} = \frac{N_{ice}}{N_{ice} + N_{liq}}, \quad (1)$$

with N_{ice} and N_{liq} the number of ice and liquid pixels, respectively. For each mixed phase cloud object, the mean size and the number of so-called ice and liquid pockets, which are respectively clusters of ice and liquid pixels, are calculated.

Clouds in the Southern Ocean can be associated with cold and warm fronts (Naud et al., 2010), stratus clouds (Hudson et al., 1998), cumulus, frontal, cirrus, and stratocumulus (Bodas-Salcedo et al., 2012). There are several criteria which enable to differentiate these cloud types, such as their fractal dimension estimated as the area-perimeter relation and defined as (Batista-Tomás et al., 2016; Lovejoy, 1982):

$$P \propto A^{\frac{D(P)}{2}} \quad (2)$$

with A the cloud area, P the perimeter, and $D(P)$ the perimeter fractal dimension. It is important to note that P represents the boundary between the cloudy and clear-sky pixels. If there are clear-sky pixels within the cloud object, they affect P and $D(P)$. For a circle or a square, $D(P)$ is equal to one but increases when the cloud shape is more complex. In the present study, to estimate the shape of each cloud object, we consider that:

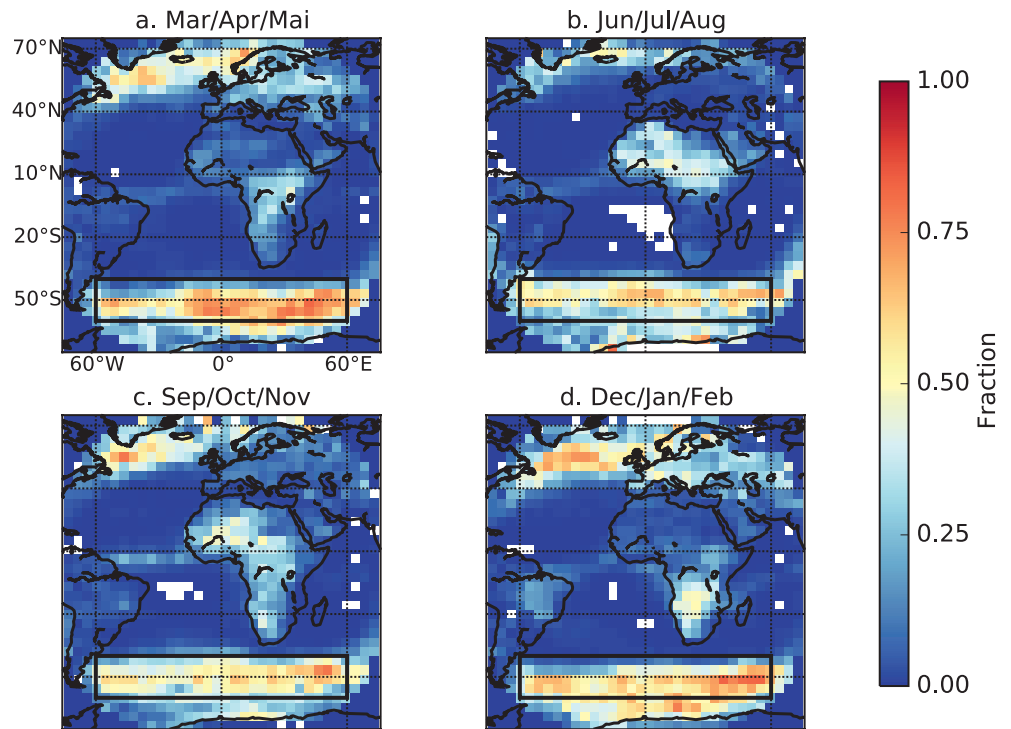


Figure 1. Mixed phase cloud fraction in 2010 over the SEVIRI disk for four different seasons: Boreal Spring (a: March, April, and May), Boreal summer (b: June, July, and August), Boreal fall (c: September, October, November), and Boreal winter (d: December, January, February). SEVIRI, Spinning Enhanced Visible and Infrared Imager.

$$D(P) = \frac{2 \ln(P)}{\ln(A)}. \quad (3)$$

If $D(P)$ is low, the cloud object shape is similar to a cumulus clouds but if $D(P)$ is high, the cloud object shape is similar to a frontal cloud (see Text S2 and Figure S1 in the supporting information for more information).

Cloud property retrieval algorithm for passive satellites do not treat mixed phase clouds as a separate category, therefore, cloud properties are retrieved considering pixels as only-liquid or only-ice. Coopman et al. (2019) have shown that pixels detected as ice by the retrievals are likely to be contaminated by liquid droplets and have an artificially low r_e^{ice} . On the opposite pixels detected as liquid but potentially contaminated by ice crystals have an artificially high r_e^{liq} . As our data set includes cloud objects for which ice pixels are in contact with liquid pixels, liquid pixels are potentially contaminated by ice crystals and vice-versa. To reduce this bias, we do not consider pixels that are at the interface between liquid and ice phase pockets within the cloud objects to reduce the likelihood of being contaminated by particle of the other phase. These pixels are not considered in retrieving cloud optical properties nor the ice fraction (cf. Equation 1). Moreover, pixels for which the uncertainty on the phase does not allow to retrieve cloud properties are discarded from the study.

4. Results and Discussion

Figure 1 shows the mixed phase cloud fraction defined as the number of mixed phase cloud objects divided by the number of all cloud objects over the SEVIRI disk for the four seasons in 2010. The spatial distribution of mixed phase at cloud top is similar to the global phase distribution shown by Korolev et al. (2017) based on CloudSat and CALIPSO observations. In the tropics, mixed phase clouds are associated with deep convective clouds and mid-level stratiform clouds. There is also a high fraction of mixed phase clouds at high

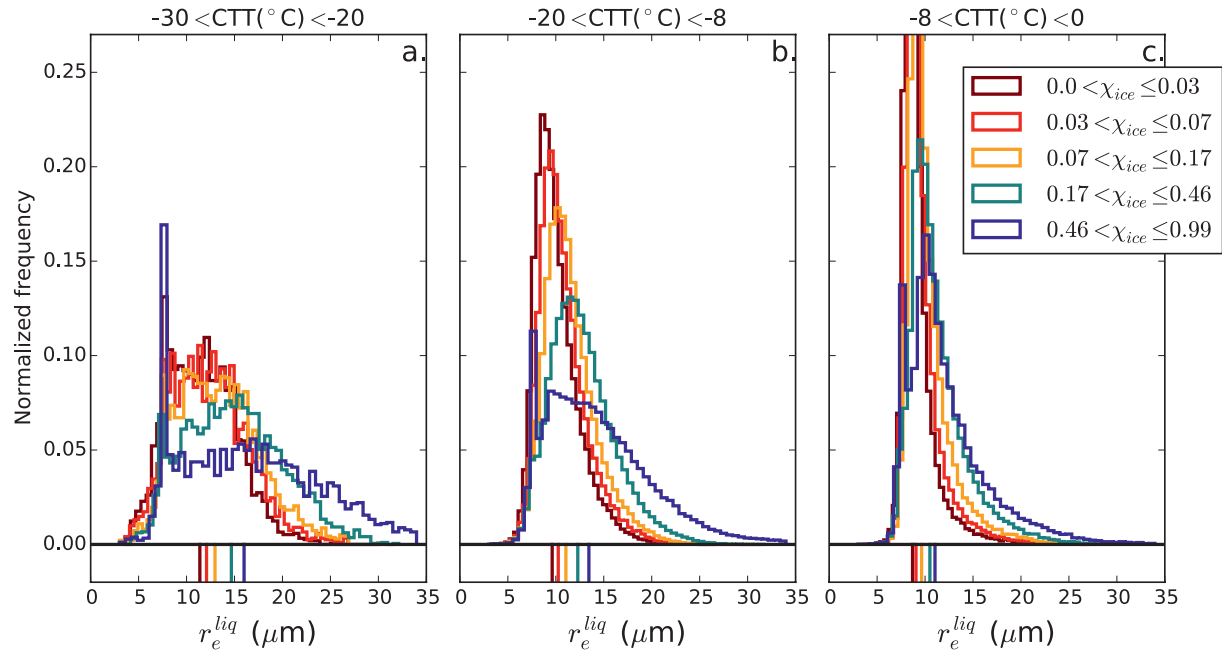


Figure 2. Cloud droplet effective radius distributions for different regimes of ice fraction defined by the 25th, 50th, and 75th percentiles and for cloud top temperatures (CTT) between -30°C and -20°C (a), between -20°C and -8°C (b), and between -8°C and 0°C (c). The colored vertical lines at the bottom of each plot denote the median values of the respective distribution.

latitudes already observed by previous studies (e.g., Intrieri, 2002; Shupe et al., 2001; Shupe et al., 2005). Mixed phase clouds are also common over the Southern Ocean (e.g., Hu et al., 2010; Huang et al., 2012; Kanitz et al., 2011) with an averaged fraction between 42% (Winter) and 48% (Spring). We focus our study on mixed phase clouds over the Southern Ocean with latitudes ranging from -60° to -40° and longitudes ranging from -60° to 60° . At these latitudes, the spatial resolution of the CLAAS-2 data set is between $4 \times 4 \text{ km}$ and $12 \times 12 \text{ km}$ with an average size of 36.5 km^2 . The minimum size of cloud objects of 30 pixels corresponds to 480 km^2 . Tan and Storelvmo (2016) studied the different liquid and ice pockets of Southern Ocean clouds with numerical simulations. The considered pocket size were between 10 m and 10 km similar to our pixel size.

Figure 2 shows r_e^{liq} constrained for χ_{ice} and for three CTT ranges: between -30°C and -20°C , between -20°C and -8°C , and between -8°C and 0°C . For the three temperature ranges, we observe that the higher the χ_{ice} , the larger the r_e^{liq} : For example, for CTT between -30°C and -20°C , the median r_e^{liq} is $11.4 \mu\text{m}$ for χ_{ice} from 0.01 to 0.03 and the median r_e^{liq} is $16.0 \mu\text{m}$ for χ_{ice} from 0.46 to 0.99. Larger cloud droplets associated with higher χ_{ice} have already been observed in previous studies (e.g., Coopman et al., 2018, 2019; Rangno & Hobbs, 2001; Rosenfeld & Lensky, 1998; Rosenfeld et al., 2011). It has been suggested that large cloud droplets are more prone to secondary ice production (Field et al., 2017) via rime splintering for temperatures between -8°C and 0°C (Hallett & Mossop, 1974). Also, large cloud droplets freeze to large ice crystals which are more prone to ice shattering. An other possible explanation is that ice is more absorbing than liquid in the near infrared so a contamination of ice crystals within a liquid-detected pixel would artificially increase the size of liquid droplets following the Nakajima and King (1990). In the current article, we do not focus on the freezing temperature (given by χ_{ice} as a function of temperature) but a short discussion can be found in Text S3 and Figure S2.

The secondary ice processes are associated with an ice multiplication mechanism (Hobbs & Rangno, 1990; Koenig, 1963) and, therefore, an increase in the ice crystal concentration (Hobbs & Rangno, 1998; Mossop, 1970; Rangno & Hobbs, 2001), which is not retrieved by algorithms based on passive sensor measurements. For liquid clouds, τ is related to droplet number concentration (N_c), mean cloud droplet size (\bar{r}) and cloud geometrical thickness (h) as (Petty, 2006):

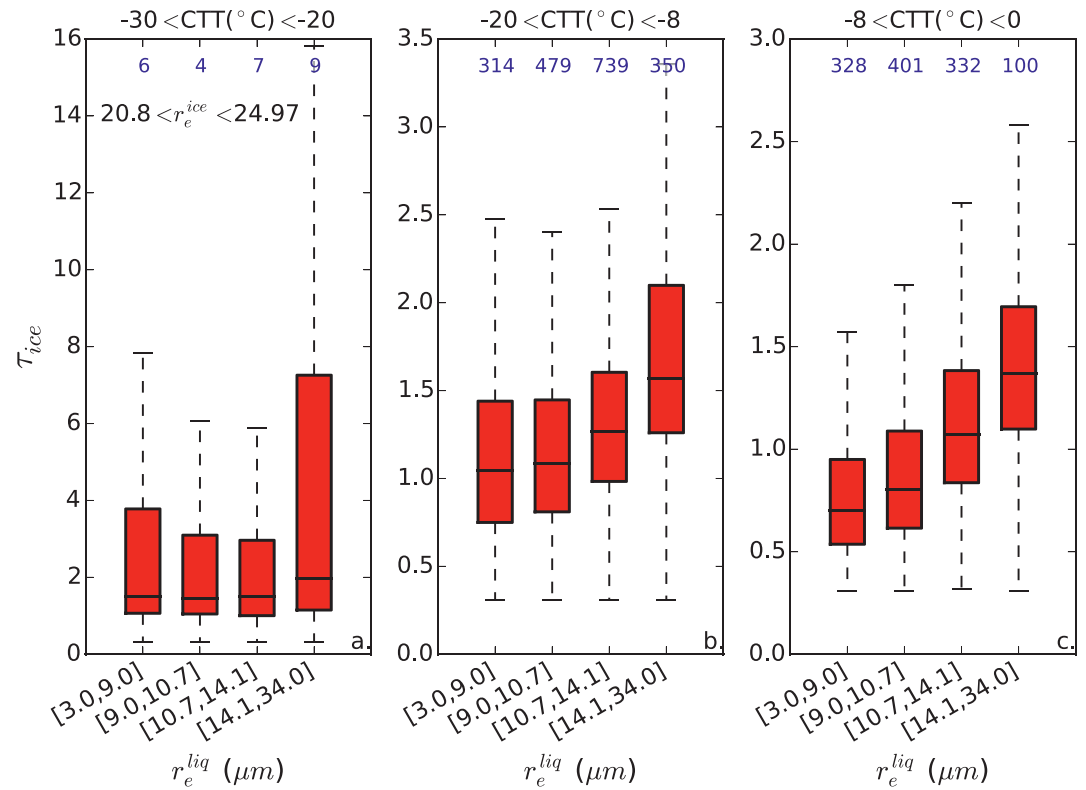


Figure 3. Variation of the optical thickness of ice pixels for different regimes of cloud droplet effective radius and constrained for the effective radius of ice crystals and cloud top temperatures. Three regimes of cloud top temperature are considered: between -30°C and -20°C (a), between -20°C and -8°C (b), and between -8°C and 0°C (c); The effective radius of ice crystals are constrained between 20.80 and 24.97 μm . For each boxplot, the central line is the median, edges of the boxes are the 25th and 75th percentiles and the dashed line extends to the 5th and 95th percentiles. The number of cloud objects included in each boxplot is indicated in blue in hundred.

$$\tau \propto N_c \bar{r}^2 h, \quad (4)$$

assuming that cloud parameters do not vary within the cloud and that r is much larger than the wavelength. Similarly, we can assume that τ of ice clouds is also proportional to the number concentration of ice crystals, \bar{r} and h . So, if we constrain for r_e^{ice} , a variation in optical thickness of ice pixels has to be associated with a variation in the cloud geometrical thickness and/or ice crystal concentration. The constrain for temperature ranges limits the impact of geometrical height on τ but we cannot rule out this dependence with the available information. It is important to note that ice number concentration cannot be retrieved from passive satellite measurements only, therefore we cannot estimate the primary nor the secondary ice number concentration. Clouds with larger cloud droplets are associated with higher ice fraction which has been speculated to be a sign of the secondary ice production by previous studies. Therefore, to support this theory, the increase in high ice fraction should be associated with an increase in ice number concentration associated here with the optical thickness of ice pixels. Figure 3 shows the optical thickness of the ice pixels as a function of r_e^{liq} of the same cloud objects for three temperature ranges and constrained for r_e^{ice} considering the first and third quartiles as thresholds to choose a narrow interval: from 21.0 to 25 μm . We observe that the optical thickness of ice pixels is increasing with r_e^{liq} for the temperature bins from -20°C to -8°C and from -8°C to 0°C and for the two regimes of r_e^{ice} . For example, for CTT between -8°C and 0°C , τ_{ice} increases from 0.7 for r_e^{liq} between 3 and 9 μm to 1.4 for r_e^{liq} between 14 and 34 μm . In contrast, for CTT between -30°C and -20°C , the optical thickness variation is smaller than for the other CTT ranges but it should be noted that the range of mean τ_{ice} is larger for the coldest CTT range than for the two other CTT ranges. We did the same analysis considering the measurement uncertainties in the optical depth rather than the

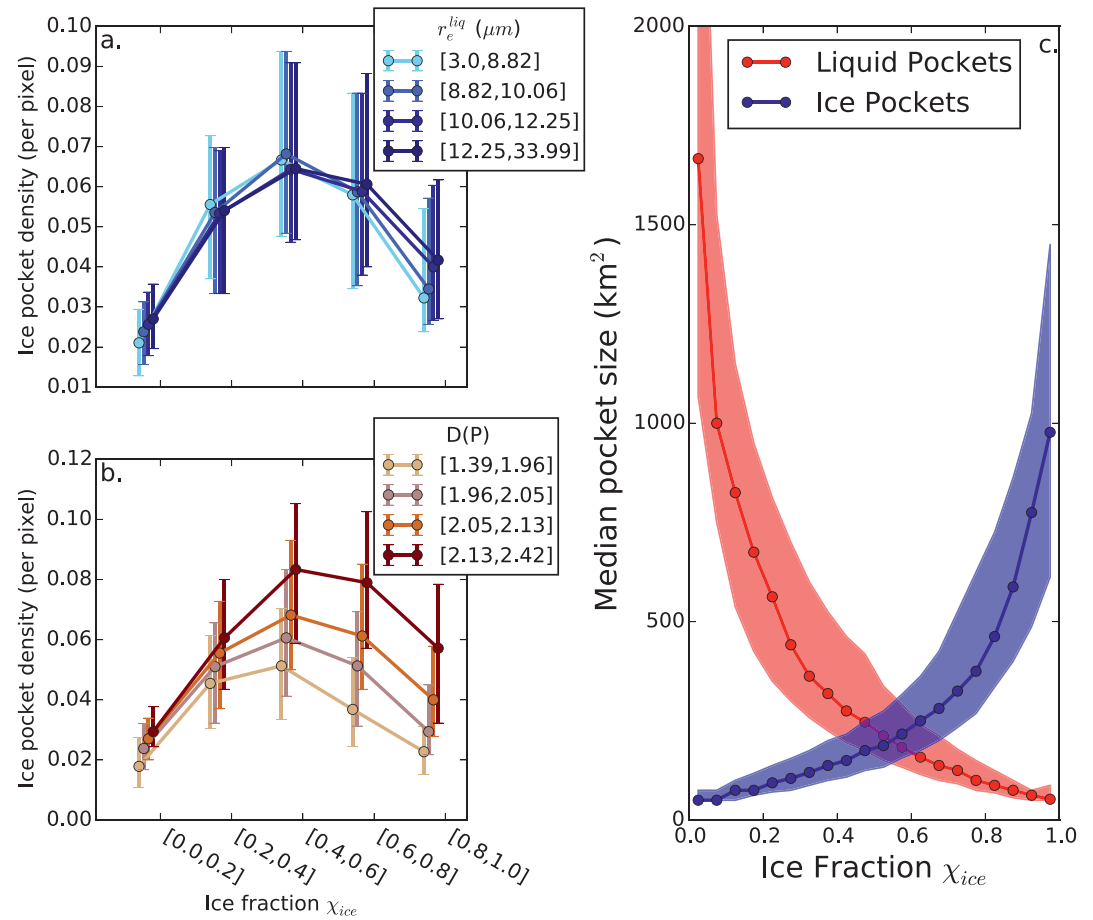


Figure 4. (a) Median of the ice pocket density as a function of ice fraction for four different regimes of r_e^{liq} defined by the 0th, 25th, 50th, 75th, and 100th percentiles. (b) Median of the ice pocket density as a function of ice fraction for four different regimes of $D(P) = \frac{2 \ln(P)}{\ln(A)}$, with P and A the cloud perimeter and area, respectively. The threshold of the regimes are defined by the 0th, 25th, 50th, 75th, and 100th percentiles of $D(P)$. The error bars indicate the 25th and 75th percentiles of the ice pocket density. (c) Median of the size of liquid (red) and ice (blue) pockets for different ice fraction regimes with the shaded areas representing the 25th and 75th percentiles.

upper and lower quartiles of the distributions and it did not change the conclusions (for more information, see Figure S3 and Text S4 in supporting information).

When regimes of r_e^{liq} lower than $9 \mu m$ and greater than $14 \mu m$ are compared, τ_{ice} increases on average by 31% for CTT between $-30 \text{ }^\circ C$ and $-20 \text{ }^\circ C$, by 50% for CTT between $-20 \text{ }^\circ C$ and $-8 \text{ }^\circ C$, and by 95% for CTT between $-8 \text{ }^\circ C$ and $0 \text{ }^\circ C$. Therefore, we speculate that the increase in ice crystal concentration with r_e^{liq} is efficient for CTT between $-8 \text{ }^\circ C$ and $0 \text{ }^\circ C$ confirming the hypothesis of active secondary ice processes associated with large cloud droplets.

We defined the ice pocket density as the number of ice pockets divided by the pixel number of the cloud (see Text S2 and Figure S1 in the supporting information for more details). Figure 4a shows the ice pocket density as a function of χ_{ice} for four regimes of r_e^{liq} . We observe that for each bin of r_e^{liq} , the increase in χ_{ice} is associated with an increase in the ice pocket density, reaches a maximum of 0.063 ice pockets per pixel for χ_{ice} between 0.4 and 0.6, and then decreases. The increase in χ_{ice} is not associated with a spread of glaciated cloud phase from pixel to pixel but rather there are multiple ice pockets not connected to each other. When χ_{ice} is greater than 0.5, ice pockets merge decreasing the ice pocket density.

We observed that higher r_e^{liq} is associated with higher ice fraction but we do not know if r_e^{liq} stimulates the number of ice pockets. Figure 4a shows that the maximum difference in ice pocket density is 0.01 per pixel for χ_{ice} between 0.8 and 1 comparing r_e^{liq} from 3.0 to 8.82 μm and from 12.25 to 33.99 μm . Thus, there seems to be no link between r_e^{liq} and the ice pocket density. So, large r_e^{liq} is associated with larger ice fraction but does not appear to stimulate the formation of ice pockets.

In the aim to better understand the evolution of ice pocket density with χ_{ice} for different types of clouds, Figure 4b shows the ice pocket density as a function of χ_{ice} for four regimes of shape parameter $D(P)$. Similarly to Figure 4a, the ice pocket density increases with χ_{ice} and reach a maximum for χ_{ice} from 0.4 to 0.6 and then decreases. We also observe that the larger $D(P)$, the higher the ice pocket density. For χ_{ice} between 0.4 and 0.6, the ice pocket density is equal to 0.05 per pixel for $D(P)$ lower than 1.96 and 0.08 per pixel for $D(P)$ greater than 2.13. Clouds with ragged boundaries are associated with a higher ice pocket density than clouds with regular boundaries. There is a correlation between the cloud size and the ice pocket density (not shown) which could explain the link between $D(P)$ and the ice pocket density. But, when the data are constrained for $D(P)$, there is no correlation between the cloud size and the ice pocket density (see Text S5 and Figure S4 in the supporting information for more details). Therefore, results from Figure 4b, do not depend on either resolution effect nor on cloud size. As the optical thickness decreases when pixels transition from liquid to ice, the pixels can become undetectable by satellite observations. $D(P)$ will increase if parts of ice pockets are undetected.

The ice pocket density increases with χ_{ice} but is the increase in density enough to explain the variation in χ_{ice} or does the ice pocket increase in size? Figure 4c shows the median pocket size for different χ_{ice} considering ice and liquid pockets. The mean ice pocket size increases from 50 to 217 km^2 with χ_{ice} increasing from 0 to 0.6 and then the ice pocket size increases to 977 km^2 for χ_{ice} equal to 0.99. The median liquid pocket size decreases from 1,667 to 183 km^2 with the χ_{ice} increasing from 0 to 0.6 and then the ice pocket size decreases to 53 km^2 for χ_{ice} equal to 0.99. When χ_{ice} is lower than 0.05, one liquid pocket and one ice pocket represents 44% and 1% of the cloud size respectively. When χ_{ice} ranges between 0.45 and 0.55, one liquid pocket and one ice pocket represents 8% and 7% of the cloud size respectively. When χ_{ice} is greater than 0.95, one liquid pocket and one ice pocket represents 2% and 40% of the cloud size respectively (see Text S6 and Figure S5 in the supporting information for more information).

From Figure 4b and 4c, we observe that the median ice pocket size and the ice pocket density increase with χ_{ice} when χ_{ice} is less than 0.6. When χ_{ice} is greater than 0.6 and the ice pocket density decreases, the increase in the median ice pocket size as a function of the χ_{ice} is steeper. On the opposite, the median liquid pocket size decreases when χ_{ice} increases and the increase in size is more rapid, possibly when the ice pockets merge with each other for χ_{ice} greater than 0.6.

5. Conclusion

We analyzed 12 years of space-based observation from the geostationary sensor SEVIRI to analyze the thermodynamic phase partitioning of the top layer of clouds over the Southern Ocean. Our results show that clouds with large droplets are associated with a higher χ_{ice} for different cloud top temperature ranges in line with previous studies (Coopman et al., 2018; Coopman, Hoose, & Stengel, 2020; Coopman, Riedi, et al., 2020; Rosenfeld & Lensky, 1998; Rangno & Hobbs, 2001; Rosenfeld et al., 2011). For the temperature ranges from -20 °C to -8 °C, and from -8 °C to 0 °C, large cloud droplets are also associated with higher optical thickness of ice pixels, while the effective radius of ice crystals is constrained, which can be used as a proxy of geometrical height or ice crystal concentration. We speculate that χ_{ice} increases with large cloud droplets can be associated with secondary ice processes for CTT ranging from -8 °C to -0 °C but further analysis are needed to confirm and quantify this effect.

We also analyzed the distribution of the ice and liquid pixels within mixed phase clouds by defining ice pockets as cluster of ice pixels. Large cloud droplets are not associated with higher density of ice pockets but clouds with a high perimeter fractal dimension are. We quantified the size of the ice pockets for different χ_{ice} . When χ_{ice} increases, the ice pocket size increases in the same time as new ice pockets are forming.

When χ_{ice} is greater than 0.5, the ice pocket size increases rapidly with χ_{ice} and the ice pockets are merging, decreasing their density.

Satellite observations allow to hypothesize on causes and consequences. We hypothesize that a variation in optical thickness of ice pixels is associated with a variation of ice crystal concentration if it is constrained for r_e^{ice} . The product LiDAR-raDAR (DARDAR) based on CALIPSO and CloudSat observations retrieves ice crystal concentration (Sourdeval et al., 2018) and can quantify the increase in ice crystal concentration associated with larger cloud droplets. Our data set and the analysis of mixed phase cloud top could be used for the evaluation and constrain of models in particular convection-permitting models to better understand the causes and the consequences of the effects discussed related to mixed phase clouds.

Data Availability Statement

The CLAAS-2 data set can be found on the following link: https://doi.org/10.5676/EUM_SAF_CM/CLAAS/V002

Acknowledgments

The authors thank two anonymous reviewers for constructive comments on the manuscript. The authors acknowledge support by the state of Baden Württemberg through bwHPC. This study has received funding from the European Research Council (ERC) under the European Union's Horizon 2020 research and innovation program (grant agreement 714062).

References

- Ahn, E., Huang, Y., Chubb, T. H., Baumgardner, D., Isaac, P., de Hoog, M., et al. (2017). In situ observations of wintertime low-altitude clouds over the Southern Ocean. *Quarterly Journal of the Royal Meteorological Society*, 143(704), 1381–1394. <https://doi.org/10.1002/qj.3011>
- Batista-Tomás, A. R., Díaz, O., Batista-Leyva, A. J., & Altshuler, E. (2016). Classification and dynamics of tropical clouds by their fractal dimension. *Quarterly Journal of the Royal Meteorological Society*, 142(695), 983–988. <https://doi.org/10.1002/qj.2699>
- Benas, N., Finkensieper, S., Stengel, M., van Zadelhoff, G.-J., Hanschmann, T., Hollmann, R., & Meirink, J. F. (2017). The MSG-SEVIRI-based cloud property data record CLAAS-2. *Earth System Science Data*, 9(2), 415–434. <https://doi.org/10.5194/essd-9-415-2017>
- Bodas-Salcedo, A., Hill, P. G., Furtado, K., Williams, K. D., Field, P. R., Manners, J. C., et al. (2016). Large contribution of supercooled liquid clouds to the solar radiation budget of the Southern Ocean. *Journal of Climate*, 29(11), 4213–4228. <https://doi.org/10.1175/jcli-d-15-0564.1>
- Bodas-Salcedo, A., Williams, K. D., Field, P. R., & Lock, A. P. (2012). The surface downwelling solar radiation surplus over the Southern Ocean in the met office model: The role of midlatitude cyclone clouds. *Journal of Climate*, 25(21), 7467–7486. <https://doi.org/10.1175/jcli-d-11-00702.1>
- Coopman, Q., Hoose, C., & Stengel, M. (2019). Detection of mixed-phase convective clouds by a binary phase information from the passive geostationary instrument SEVIRI. *Journal of Geophysical Research: Atmospheres*, 124(9), 5045–5057. <https://doi.org/10.1029/2018jd029772>
- Coopman, Q., Hoose, C., & Stengel, M. (2020). Analysis of the thermodynamic phase transition of tracked convective clouds based on geostationary satellite observations. *Journal of Geophysical Research: Atmospheres*, 125(11). <https://doi.org/10.1029/2019JD032146>
- Coopman, Q., Riedi, J., Finch, D. P., & Garrett, T. J. (2018). Evidence for changes in arctic cloud phase due to long-range pollution transport. *Geophysical Research Letters*, 45(19), 10709–10718. <https://doi.org/10.1029/2018gl079873>
- Coopman, Q., Riedi, J., Zeng, S., & Garrett, T. J. (2020). Space-based analysis of the cloud thermodynamic phase transition for varying microphysical and meteorological regimes. *Geophysical Research Letters*, 47(6). <https://doi.org/10.1029/2020gl087122>
- Curry, J. A., Hobbs, P. V., King, M. D., Randall, D. A., Minnis, P., Isaac, G. A., et al. (2000). FIRE Arctic Clouds Experiment. *Bulletin of the American Meteorological Society*, 81(1), 5–29. [https://doi.org/10.1175/1520-0477\(2000\)081<0005:face>2.3.co;2](https://doi.org/10.1175/1520-0477(2000)081<0005:face>2.3.co;2)
- Dee, D. P., Uppala, S. M., Simmons, a. J., Berrisford, P., Poli, P., Kobayashi, S., et al. (2011). The ERA-Interim reanalysis: Configuration and performance of the data assimilation system. *Quarterly Journal of the Royal Meteorological Society*, 137(656), 553–597. <https://doi.org/10.1002/qj.828>
- Field, P. R., Lawson, R. P., Brown, P. R. A., Lloyd, G., Westbrook, C., Moisseev, D., et al. (2017). Secondary ice production—Current state of the science and recommendations for the future. In *Ice formation and evolution in clouds and precipitation: Measurement and modeling challenges* (Meteorological Monographs, Chapter 7, pp. 7.1–7.20). <https://doi.org/10.1175/AMSMONOGRAPHS-D-16-0014.1>
- Gettelman, A., & Sherwood, S. C. (2016). Processes responsible for cloud feedback. *Current Climate Change Reports*, 2(4), 179–189. <https://doi.org/10.1007/s40641-016-0052-8>
- Grosvenor, D. P., & Wood, R. (2014). The effect of solar zenith angle on MODIS cloud optical and microphysical retrievals within marine liquid water clouds. *Atmospheric Chemistry and Physics*, 14(14), 7291–7321. <https://doi.org/10.5194/acp-14-7291-2014>
- Hallett, J., & Mossop, S. C. (1974). Production of secondary ice particles during the riming process. *Nature*, 249(5452), 26–28. <https://doi.org/10.1038/249026a0>
- Hobbs, P. V., & Rangno, A. L. (1990). Rapid development of high ice particle concentrations in small polar maritime cumuliform clouds. *Journal of the Atmospheric Sciences*, 47(22), 2710–2722. [https://doi.org/10.1175/1520-0469\(1990\)047<2710:rdohip>2.0.co;2](https://doi.org/10.1175/1520-0469(1990)047<2710:rdohip>2.0.co;2)
- Hobbs, P. V., & Rangno, A. L. (1998). Microstructures of low and middle-level clouds over the Beaufort Sea. *Quarterly Journal of the Royal Meteorological Society*, 124, 2035–2071. <https://doi.org/10.1002/qj.49712455012>
- Hu, Y., Rodier, S., Xu, K.-m., Sun, W., Huang, J., Lin, B., et al. (2010). Occurrence, liquid water content, and fraction of supercooled water clouds from combined CALIOP/IIR/MODIS measurements. *Journal of Geophysical Research*, 115(19), D00H34. <https://doi.org/10.1029/2009jd012384>
- Huang, Y., Siems, S. T., Manton, M. J., Protat, A., & Delanoë, J. (2012). A study on the low-altitude clouds over the Southern Ocean using the DARDAR-MASK. *Journal of Geophysical Research*, 117(D18). <https://doi.org/10.1029/2012jd017800>
- Hudson, J. G., Xie, Y., & Yum, S. S. (1998). Vertical distributions of cloud condensation nuclei spectra over the summertime Southern Ocean. *Journal of Geophysical Research*, 103(D13), 16609–16624. <https://doi.org/10.1029/97jd03438>
- Intrieri, J. M. (2002). An annual cycle of Arctic cloud characteristics observed by radar and lidar at SHEBA. *Journal of Geophysical Research*, 107(C10), 8030. <https://doi.org/10.1029/2000jc000423>

- Kanitz, T., Seifert, P., Ansmann, A., Engelmann, R., Althausen, D., Casiccia, C., & Rohwer, E. G. (2011). Contrasting the impact of aerosols at northern and southern midlatitudes on heterogeneous ice formation. *Geophysical Research Letters*, *38*(17). <https://doi.org/10.1029/2011gl048532>
- Koenig, L. R. (1963). The glaciating behavior of small cumulonimbus clouds. *Journal of the Atmospheric Sciences*, *20*(1), 29–47. [https://doi.org/10.1175/1520-0469\(1963\)020<0029:tgbsoc>2.0.co;2](https://doi.org/10.1175/1520-0469(1963)020<0029:tgbsoc>2.0.co;2)
- Korolev, A., McFarquhar, G., Field, P. R., Franklin, C., Lawson, P., Wang, Z., et al. (2017). Mixed-phase clouds: Progress and challenges. *Meteorological Monographs*, *58*(5), 1–5. <https://doi.org/10.1175/amsmonographs-d-17-0001.1>
- Lovejoy, S. (1982). Area-perimeter relation for rain and cloud areas. *Science*, *216*(4542), 185–187. <https://doi.org/10.1126/science.216.4542.185>
- Mültenstädt, J., Sourdeval, O., Delanoë, J., & Quaas, J. (2015). Frequency of occurrence of rain from liquid-, mixed-, and ice-phase clouds derived from A-Train satellite retrievals. *Geophysical Research Letters*, *42*(15), 6502–6509. <https://doi.org/10.1002/2015GL064604>
- Mace, G. G., Benson, S., & Hu, Y. (2020). On the frequency of occurrence of the ice phase in supercooled Southern Ocean low clouds derived from CALIPSO and CloudSat. *Geophysical Research Letters*, *47*(14), 1–8. <https://doi.org/10.1029/2020GL087554>
- Mace, G. G., & Protat, A. (2018). Clouds over the Southern Ocean as observed from the r/v investigator during CAPRICORN. Part I: Cloud occurrence and phase partitioning. *Journal of Applied Meteorology and Climatology*, *57*(8), 1783–1803. <https://doi.org/10.1175/jamc-d-17-0194.1>
- Mace, G. G., Protat, A., Humphries, R. S., Alexander, S. P., McRobert, I. M., Ward, J., et al. (2020). Southern Ocean cloud properties derived from CAPRICORN and MARCUS data. *Journal of Geophysical Research: Atmospheres*, *126*. <https://doi.org/10.1029/2020jd033368>
- Matricardi, M., Chevallier, F., Kelly, G., & Thépaut, J.-N. (2004). An improved general fast radiative transfer model for the assimilation of radiance observations. *Quarterly Journal of the Royal Meteorological Society*, *130*(596), 153–173. <https://doi.org/10.1256/qj.02.181>
- McCoy, D. T., & Hartmann, D. L. (2015). Observations of a substantial cloud-aerosol indirect effect during the 2014–2015 Barabunga-Veiivotn fissure eruption in Iceland. *Geophysical Research Letters*, *42*(23), 10409–10414. <https://doi.org/10.1002/2015gl067070>
- McCoy, D. T., Tan, I., Hartmann, D. L., Zelinka, M. D., & Storelvmo, T. (2016). On the relationships among cloud cover, mixed-phase partitioning, and planetary albedo in GCMs. *Journal of Advances in Modeling Earth Systems*, *8*(2), 650–668. <https://doi.org/10.1002/2015ms000589>
- McFarquhar, G. M., Bretherton, C., Marchand, R., Protat, A., DeMott, P. J., Alexander, S. P., et al. (2020). Observations of clouds, aerosols, precipitation, and surface radiation over the Southern Ocean: An overview of CAPRICORN, MARCUS, MICRE and SOCRATES. *Bulletin of the American Meteorological Society*, 1–92. <https://doi.org/10.1175/bams-d-20-0132.1>
- Meirink, J. F., Roebeling, R. A., & Stammes, P. (2013). Inter-calibration of polar imager solar channels using SEVIRI. *Atmospheric Measurement Techniques*, *6*(9), 2495–2508. <https://doi.org/10.5194/amt-6-2495-2013>
- Meirink, J. F., & van Zadelhoff, G. J. (2016). *Algorithm theoretical basis document, SEVIRI cloud physical products, CLAAS edition 2* (Technical Report No. 2.2). Offenbach, Germany: EUMETSAT Satellite Application Facility on Climate Monitoring. https://doi.org/10.5676/EUM_SAF_CM/CLAAS/V002
- Menzel, W. P., Smith, W. L., & Stewart, T. R. (1983). Improved cloud motion wind vector and altitude assignment using VAS. *Journal of Climate and Applied Meteorology*, *22*(3), 377–384. [https://doi.org/10.1175/1520-0450\(1983\)022<0377:icmwva>2.0.co;2](https://doi.org/10.1175/1520-0450(1983)022<0377:icmwva>2.0.co;2)
- Mossop, S. C. (1970). Concentrations of ice crystals in clouds. *Bulletin of the American Meteorological Society*, *51*. [https://doi.org/10.1175/1520-0477\(1970\)051<0474:coicic>2.0.co;2](https://doi.org/10.1175/1520-0477(1970)051<0474:coicic>2.0.co;2)
- Nakajima, T., & King, M. D. (1990). Determination of the optical thickness and effective particle radius of clouds from reflected solar radiation measurements. Part I: Theory. *Journal of the Atmospheric Sciences*, *47*(15), 1878–1893. [https://doi.org/10.1175/1520-0469\(1990\)047<1878:dotota>2.0.co;2](https://doi.org/10.1175/1520-0469(1990)047<1878:dotota>2.0.co;2)
- Naud, C. M., Booth, J. F., & Del Genio, A. D. (2014). Evaluation of ERA-Interim and MERRA cloudiness in the Southern Ocean. *Journal of Climate*, *27*(5), 2109–2124. <https://doi.org/10.1175/JCLI-D-13-00432.1>
- Naud, C. M., Del Genio, A. D., Bauer, M., & Kovari, W. (2010). Cloud vertical distribution across warm and cold fronts in cloudsat-CALIPSO data and a general circulation model. *Journal of Climate*, *23*(12), 3397–3415. <https://doi.org/10.1175/2010JCLI3282.1>
- Noh, Y. J., Miller, S. D., Heiding, A. K., Mace, G. G., Protat, A., & Alexander, S. P. (2019). Satellite-based detection of daytime supercooled liquid-topped mixed-phase clouds over the Southern Ocean Using the advanced Himawari Imager. *Journal of Geophysical Research: Atmospheres*, *124*(5), 2677–2701. <https://doi.org/10.1029/2018JD029524>
- Petty, G. W. (2006). *A first course in atmospheric radiation*. Sundog Pub.
- Rangno, A. L., & Hobbs, P. V. (2001). Ice particles in stratiform clouds in the Arctic and possible mechanisms for the production of high ice concentrations. *Journal of Geophysical Research*, *106*(D14), 15065–15075. <https://doi.org/10.1029/2000jd900286>
- Roebeling, R. A., Feijt, A. J., & Stammes, P. (2006). Cloud property retrievals for climate monitoring: Implications of differences between Spinning Enhanced Visible and Infrared Imager (SEVIRI) on METEOSAT-8 and Advanced Very High Resolution Radiometer (AVHRR) on NOAA-17. *Journal of Geophysical Research*, *111*(D20), D20210. <https://doi.org/10.1029/2005jd006990>
- Rosenfeld, D., & Lensky, I. M. (1998). Satellite-based insights into precipitation formation processes in continental and maritime convective clouds. *Bulletin of the American Meteorological Society*, *79*(11), 2457–2476. [https://doi.org/10.1175/1520-0477\(1998\)079<2457:sbiipf>2.0.co;2](https://doi.org/10.1175/1520-0477(1998)079<2457:sbiipf>2.0.co;2)
- Rosenfeld, D., Yu, X., Liu, G., Xu, X., Zhu, Y., Yue, Z., et al. (2011). Glaciation temperatures of convective clouds ingesting desert dust, air pollution and smoke from forest fires. *Geophysical Research Letters*, *38*(21), L21804. <https://doi.org/10.1029/2011gl049423>
- Saunders, R., Matricardi, M., & Brunel, P. (1999). An improved fast radiative transfer model for assimilation of satellite radiance observations. *Quarterly Journal of the Royal Meteorological Society*, *125*(556), 1407–1425. <https://doi.org/10.1002/qj.1999.49712555615>
- Schäfer, M., Loewe, K., Ehrlich, A., Hoese, C., & Wendisch, M. (2018). Simulated and observed horizontal inhomogeneities of optical thickness of Arctic stratus. *Atmospheric Chemistry and Physics*, *18*(17), 13115–13133. <https://doi.org/10.5194/acp-18-13115-2018>
- Schmetz, J., Holmlund, K., Hoffman, J., Strauss, B., Mason, B., Gaertner, V., et al. (1993). Operational cloud-motion winds from meteosat infrared images. *Journal of Applied Meteorology*, *32*(7), 1206–1225. [https://doi.org/10.1175/1520-0450\(1993\)032<1206:ocmwim>2.0.co;2](https://doi.org/10.1175/1520-0450(1993)032<1206:ocmwim>2.0.co;2)
- Shupe, M. D., Daniel, J. S., de Boer, G., Eloranta, E. W., Kollias, P., Long, C. N., et al. (2008). A focus on mixed-phase clouds. *Bulletin of the American Meteorological Society*, *89*(10), 1549–1562. <https://doi.org/10.1175/2008bams2378.1>
- Shupe, M. D., Uttal, T., & Matrosov, S. Y. (2005). Arctic cloud microphysics retrievals from surface-based remote sensors at SHEBA. *Journal of Applied Meteorology*, *44*(10), 1544–1562. <https://doi.org/10.1175/jam2297.1>
- Shupe, M. D., Uttal, T., Matrosov, S. Y., & Frisch, A. S. (2001). Cloud water contents and hydrometeor sizes during the FIRE Arctic Cloud Experiment. *Journal of Geophysical Research*, *106*(D14), 15015–15028. <https://doi.org/10.1029/2000jd900476>

- Sourdeval, O., Gryspeerdt, E., Krämer, M., Goren, T., Delanoë, J., Afchine, A., et al. (2018). Ice crystal number concentration estimates from lidar-radar satellite remote sensing—Part 1: Method and evaluation. *Atmospheric Chemistry and Physics*, *18*(19), 14327–14350. <https://doi.org/10.5194/acp-18-14327-2018>
- Stammes, P. (2001). Spectral radiance modelling in the UV-Visible range. In W. L. Smith, & Y. M. Timofeyev (Eds.), *Irs 2000: Current problems in atmospheric radiation* (pp. 385–388). Hampton, VA: A. Deepak Publ.
- Stengel, M., Kniffka, A., Meirink, J. F., Lockhoff, M., Tan, J., & Hollmann, R. (2014). CLAAS: The CM SAF cloud property data set using SEVIRI. *Atmospheric Chemistry and Physics*, *14*(8), 4297–4311. <https://doi.org/10.5194/acp-14-4297-2014>
- Stengel, M., Schlundt, C., Stapelberg, S., Sus, O., Eliasson, S., Willén, U., & Meirink, J. F. (2018). Comparing ERA-Interim clouds with satellite observations using a simplified satellite simulator. *Atmospheric Chemistry and Physics*, *18*(23), 17601–17614. <https://doi.org/10.5194/acp-18-17601-2018>
- Sun, Z., & Shine, K. P. (1994). Studies of the radiative properties of ice and mixed-phase clouds. *Quarterly Journal of the Royal Meteorological Society*, *120*(515), 111–137. <https://doi.org/10.1002/qj.49712051508>
- Tan, I., & Storelvmo, T. (2016). Sensitivity study on the influence of cloud microphysical parameters on mixed-phase cloud thermodynamic phase partitioning in CAM5. *Journal of the Atmospheric Sciences*, *73*(2), 709–728. <https://doi.org/10.1175/jas-d-15-0152.1>
- Tan, I., Storelvmo, T., & Choi, Y.-S. (2014). Spaceborne lidar observations of the ice-nucleating potential of dust, polluted dust, and smoke aerosols in mixed-phase clouds. *Journal of Geophysical Research: Atmospheres*, *119*(11), 6653–6665. <https://doi.org/10.1002/2013jd021333>
- Tan, I., Storelvmo, T., & Zelinka, M. D. (2016). Observational constraints on mixed-phase clouds imply higher climate sensitivity. *Science*, *352*(6282), 224–227. <https://doi.org/10.1126/science.aad5300>
- Vergara-Temprado, J., Miltenberger, A. K., Furtado, K., Grosvenor, D. P., Shipway, B. J., Hill, A. A., et al. (2018). Strong control of Southern Ocean cloud reflectivity by ice-nucleating particles. *Proceedings of the National Academy of Sciences of the United States of America*, *115*(11), 2687–2692. <https://doi.org/10.1073/pnas.1721627115>
- Wang, Z., Vane, D., Stephens, G., & Reinke, D. (2003). *Level 2 combined radar and lidar cloud scenario classification product process description and interface control document* (Technical Report No. 1.0). Pasadena, CA: Jet Propulsion Laboratory. Retrieved from <http://scholar.google.com/scholar?hl=en&btnG=Search&q=intitle:Level+2+Combined+Radar+and+Lidar+Cloud+Scenario+Classification+Product+Process+Description+and+Interface+Control+Document#1>